Chromophore–dependent Intramolecular Exciton–Vibrational Coupling in the FMO Complex: Quantification and Importance for Exciton Dynamics

Daniele Padula,*,† Myeong H. Lee,† Kirsten Claridge,† and Alessandro Troisi†,‡

†*Department of Chemistry, University of Warwick, Coventry CV4 7AL, UK*

‡*Materials Innovation Factory, University of Liverpool, Liverpool L69 7ZD, UK*

E-mail: d.padula@warwick.ac.uk

Phone: +44 24765 74623

Abstract

In this paper we adopt an approach suitable for monitoring the time evolution of the intramolecular contribution to the spectral density of a set of identical chromophores embedded in their respective environments. We apply the proposed method to the Fenna–Matthews–Olson (FMO) complex, with the objective to quantify the differences among site–dependent spectral densities and the impact of such differences on the exciton dynamics of the system. Our approach is based on the one recently proposed in *J. Phys. Chem. Lett.*, **2016**, *7*, 3171–3178 and takes advantage of the Vertical Gradient approximation to reduce the computational demands of the normal modes analysis. We show that the region of the spectral density that is believed to strongly influence the exciton dynamics changes significantly over a large time scale. We then studied the impact of the intramolecular vibrations on the exciton dynamics by considering a model of FMO in a vibronic basis and neglecting the interaction with the environment to isolate the role of the intramolecular exciton-vibration coupling. In agreement with the assumptions in the literature, we demonstrate that high frequency modes at energy much larger than the excitonic energy splitting have negligible influence on exciton dynamics despite the large exciton-vibration coupling. We also find that the impact of including the site–dependent spectral densities on exciton dynamics is not very significant, indicating that it may be acceptable to apply the same spectral density on all sites. However, care needs to be taken for the description of the exciton–vibrational coupling in the low frequency part of intramolecular modes because exciton dynamics is more susceptible to low frequency modes despite their small Huang-Rhys factors.

1 Introduction

When trying to understand the physics of energy transfer in Light Harversting Complexes (LHCs),[1–3] a number of authors have tried, on one hand, to build models as realistic as possible[4–14] and, on the other hand, to capture the essence of the phenomenon with model Hamiltonians containing a reduced number of parameters.[15–20] Ideally, one wants to understand the system in terms of the simplest possible model that captures the physics explaining a range of experiments. The coupling between exciton and high frequency vibrations localised on each chromophore is a highly debated point in recent works as it has been proposed that such coupling is essential for efficient energy transfer.[21–27] Moreover, the inclusion of high frequency intramolecular vibrations greatly complicates the description of the quantum dynamics, giving rise to non-Markovian effects (if the vibrations are part of the bath) or very large Liouville space (if the vibrations are included in the sytem). The aim of this work is to present a detailed calculation of the intramolecular exciton–vibrational coupling in multichromophoric systems and an assessment of the level of detail needed to describe the quantum dynamics of the exciton.

A common way to evaluate the spectral density of a chromophore embedded in a protein involves the Fourier Transform of the autocorrelation function of the excitation energy.[1] This is computed by sampling a classical molecular dynamics (MD) trajectory at very small time intervals, so that the high frequency region of the spectral density can be retrieved, and for several picoseconds, so that the low frequency region is described accurately. A set of snapshots is then extracted from the classical MD trajectory, and excitation energies are computed for each snapshot at various levels of accuracy, usually including the environment in a classical scheme (point charges),[4,5,7,9,10,12] sometimes even taking polarisation effects into account.[1,8,13,14] The major problem involving this approach is the inconsistency between the potentials used to estimate the electronic–nuclear coupling and the excitation energies, leading to inaccurate descriptions.[28,29] Other problems related to the nature of this approach, such as the choice of the classical force–field,[30] the so–called "geometry mismatch",[1] the

treatment of quantised (intramolecular) vibrations in a classical framework,[11] can lead to further inaccuracies. The methodology is also extremely expensive computationally, forcing most users to adopt semiempirical quantum chemical methods (like ZINDO)[4,5,8,9,12,14] or investing such a large amount of resources that makes the calculations difficult to repeat or modify. The procedure described leads to an analysis limited to small time intervals (tens of picoseconds at best), making it virtually impossible to evaluate the evolution of the electron-phonon coupling on a time scale where conformational rearrangements of the protein may occur.

The objective of this paper is to monitor the time evolution of the intramolecular part of the spectral density of a set of identical chromophores embedded in their respective environments, starting from other approaches and approximations that have been proposed recently.[28,29,31] For this purpose, we will focus on the most studied LHC, namely the Fenna–Matthews–Olson (FMO) complex. We computed the spectral densities for each chromophore over a large time scale to highlight the differences of this strategy in comparison to MD–based approaches. The spectral densities are then used to extract a set of effective frequencies (Sec. 2.1) to describe in a vibronic basis the dynamics of the excitation within the closed excitonic system (Sec. 2.2). This will provide insight as to whether the high frequency part of intramolecular modes has a negligible influence on the exciton dynamics for this system. Finally, we evaluate the differences among the set of site–dependent spectral densities in terms of impact on the physics of the system.

2 Results and Discussion

2.1 Computation of the exciton–vibrational coupling

It is possible to improve the consitency between the classical and the quantum–mechanical (QM) potential and to solve, at least partially, some of the problems discussed in the Introduction. For instance, to avoid the "geometry mismatch" problem it is possible to run expen-

sive quantum–mechanics/molecular–mechanics (QM/MM) MD simulations,[14] or to project QM optimised structures onto the MD geometries with an RMSD minimisation procedure.[32] An alternative would be to parametrise the MM force–fields so that they reproduce the QM behaviour.[33,34] A different solution involves the separation of the spectral density into intra– and intermolecular contributions.[28,29,31] In refs.[28,29], Lee and Coker devised a strategy to compute the intramolecular contributions (the ones that classical potentials describe inaccurately[11]) at a high level of accuracy: assuming that the harmonic approximation holds in both electronic states and that the vibrational motions and frequencies are the same in the two electronic states, they propose a procedure to map the ground state Potential Energy Surface (PES) to the excited state one, by monitoring the slope of the excitation energy gap upon distortion of the ground state geometry along a normal mode coordinate. In this way, it is possible to retrieve the displacement from the equilibrium position along each normal mode, and thus the Huang–Rhys factor and the reorganisation energy. These are the needed quantities to obtain the intramolecular part of the spectral density,[28] as in

$$J(\omega) = \pi \sum_i \omega_i \lambda_i \delta(\omega - \omega_i), \tag{1}$$

where ω_i and λ_i are the frequency and reorganisation energy of the i-th normal mode, respectively. While the strategy proposed resulted in an impressive agreement with experimental data, its numerical implementation is nonetheless computationally demanding, since it involves distortion of the geometry along each normal mode coordinate for an arbitrarily chosen number of points, followed by an excited state calculation. The nature of the approach leaves space for easy automatisation, but the number of TDDFT calculations to be run is still of the order of at least several thousands.

Starting from the same assumptions (harmonic approximation, same frequencies and normal modes in both electronic states), it is possible to use the so–called "Vertical Gradient" (VG) approximation,[35,36] which allows the approximation of the full excited state PES from a single gradient calculation at the Franck–Condon point of the ground state equilibrium

geometry. The method, also known with the names "Linear Coupling Model" (LCM)[37] or "Vertical Franck–Condon" (VFC),[38] has been widely applied[35–42] and is particularly useful for molecules for which a geometry optimisation in the excited state is either difficult or computationally unfeasible.[39] Within the harmonic approximation we can write the electronic ground state (GS) PES as[35,36]

$$E_{GS}(\mathbf{Q}_{GS}) = \frac{1}{2}\mathbf{Q}_{GS}^T \mathbf{\Omega}_{GS}^2 \mathbf{Q}_{GS}, \tag{2}$$

where $\mathbf{Q}_{GS}$ is the vector of ground state normal modes (expressed in mass-weighted coordinates), and $\mathbf{\Omega}_{GS}$ is the diagonal matrix of ground state vibrational frequencies. For the electronic excited state (ES) PES, we consider a truncated Taylor expansion about the GS equilibrium position, as in

$$E_{ES}(\mathbf{Q}_{GS}) = \Delta E_v + (\nabla E_{ES})^T \mathbf{Q}_{GS} + \frac{1}{2}\mathbf{Q}_{GS}^T \mathbf{H}_{ES} \mathbf{Q}_{GS}, \tag{3}$$

where ΔE_v is the vertical energy difference at the ground state minimum, ∇E_{ES} is the vector of excited state gradients along each normal mode at the ground state minimum, and with $\mathbf{H}_{ES}$ we indicate the excited state Hessian. The Hessian is, in general, not diagonal, *i.e.* the normal modes of the excited state ($\mathbf{Q}_{ES}$) can be expressed in terms of the ones of the ground state according to[43]

$$\mathbf{Q}_{ES} = \mathbf{J}\mathbf{Q}_{GS} + \mathbf{K}, \tag{4}$$

where $\mathbf{J}$ is the Duschinsky matrix and $\mathbf{K}$ the displacement vector. If we assume that the normal modes and the vibrational frequencies in the two states are the same, we are setting $\mathbf{J} = \mathbb{1}$ and we can replace $\mathbf{H}_{ES}$ in Eq. 3 by $\mathbf{\Omega}_{GS}^2$. We thus need to determine the displacement vector $\mathbf{K}$, which, following Santoro,[35] we can express in terms of the excited state gradient at the ground state minimum as in

$$\mathbf{K} = -\mathbf{\Omega}_{GS}^{-2} \nabla E_{ES}. \tag{5}$$

It is convenient to convert the mass-weighted displacements to dimensionless units,[44] using $\Delta_i = K_i \sqrt{\frac{\omega_i}{\hbar}}$, where ω_i is the frequency of the i-th normal mode. We obtained the Huang–Rhys factor $S_i = \frac{1}{2}\Delta_i^2$ and the reorganisation energy $\lambda_i = \hbar\omega_i S_i$ for the i-th normal mode, and the total one as $\lambda = \sum_{i=1}^{3N-6} \lambda_i$.

To summarise, the model requires the knowledge of the ground state equilibrium geometry, normal modes ($\mathbf{Q}_{GS}$) and vibrational frequencies ($\mathbf{\Omega}_{GS}$), and of the excited state gradients at the ground state equilibrium geometry (∇E_{ES}). All these quantities can be obtained in a QM framework, even considering environmental effects with continuum (PCM,[45] COSMO[46]) or atomistic models (ONIOM,[47] QM/MM[1]). The latter in particular allows the consideration of the differences that might characterise identical chromophores embedded in different environments, allowing to study the spectral density of local minima visited along the trajectory. More details on the protocol followed to obtain the required data for the vibrational analysis are given in Sec. 4. This approximation is appropriate because bacteriochlorophyll–A (BCL) molecules do not undergo large amplitude motions upon electronic excitation. To conclude this overview, we stress that the basic assumptions of the model are exactly the same used in MD–based approaches, namely a linear coupling of the excitation with an harmonic bath. The major advantages in comparison to MD–based methods are: (i) a faster evaluation of the spectral density (ii) a more realistic description of intramolecular modes (iii) the possibility to study environmental effects over very large time scales, that may involve conformational rearrangements of the protein.

We implemented the VG approach to calculate the displacements, the Huang–Rhys factors, and reorganisation energies for the 8 BCLs in a monomeric unit of FMO, including environmental effects in an ONIOM scheme (see Sec. 4), similarly to what proposed in ref.[28]. The ONIOM approach results particularly convenient in the geometry optimisation process in comparison to QM/MM microiteration approaches because of subtle difficulties

that the latter may present, such as an excessive proximity between QM atoms and point charges. However, one major drawback of the ONIOM approach is the lack of inclusion of any polarisation effect whatsoever. For a more accurate description of a process involving an electronic rearrangement, better results could be obtained using an approach that takes into account polarisation of the QM density due to an electrostatic embedding rather than the ONIOM approach, which can be further improved considering mutual polarisation approaches. Table 1 shows the values we obtained from the normal modes analysis within the VG framework, and it shows the difference with respect to gas phase calculations. The agreement with experimental data from Difference Fluorescence Line Narrowing (ΔFLN) performed on FMO at low temperature[48] is reasonable, validating the VG approximation for this molecule. There is a clear tendency in underestimating the total reorganisation energy, which can be explained considering the lack of polarisation effects intrinsic to the ONIOM description discussed a few lines above. Finally, the computed values agree with other literature data on the same[49] or on similar chromophores.[31]

Table 1: Total reorganisation energies (λ) obtained from the normal modes analysis in a VG framework.

Chrom.	Env.	λ (cm^{-1})
ΔFLN exp.[48]		209
BCL	gas phase	128
BCL367	ONIOM	152
BCL368	ONIOM	149
BCL369	ONIOM	167
BCL370	ONIOM	152
BCL371	ONIOM	135
BCL372	ONIOM	136
BCL373	ONIOM	147
BCL400	ONIOM	147

From the normal modes analysis, we computed the spectral densities convolving the discrete line spectrum (see Eq. 1) with a continuous lineshape function describing the response of a Brownian harmonic oscillator to an external field[50]

$$J(\omega) = \pi \sum_{i=1}^{3N-6} \omega_i \lambda_i \frac{\gamma\omega^2}{(\gamma\omega)^2 + (\omega_i^2 - \omega^2)^2} \tag{6}$$

where ω_i and λ_i are the frequency and reorganisation energy of the i-th normal mode, respectively, and γ is a broadening parameter arbitrarily chosen. Out of simplicity, we used the same γ for all normal modes, convolving the discrete spectrum with $\gamma = 5$ cm^{-1} for comparison with data obtained at different times (see Figs. 1 and 2), and $\gamma = 125$ cm^{-1} to extract a coarse–grained model of the spectral density (see Fig. 3), assuming it is the result of a small number of damped harmonic oscillators, to use in the study of the exciton dynamics.

In Fig. 1 we show the comparison between spectral densities separated by an 8 ns time window. The spectral densities of the eight chromophores show very similar profiles. In all cases, the 1200–1400 cm^{-1} region is rich of highly contributing modes characterised by combined stretching and in–plane bending motions of the ring. A lower contribution can be identified in the 700–800 cm^{-1} region, where the ring is involved in combined bending vibrations. The main feature that we can identify in these regions due to time evolution is the redistribution of the coupling with the excitation, but the modes involved seem to be the same. BCL367 seems to be the chromophore with the most significant variations in terms of frequency of the modes involved and intensity of the coupling. The region below 500 cm^{-1} is characterised by out-of-plane motions involving the whole ring. This last region is the one that is more influenced by the time evolution (*i.e.* environmental rearrangements) and, as assumed in the literature and demonstrated in the second part of this paper, it is the region that influences the most the exciton dynamics.

A visual comparison with computed spectral densities reported by Coker[28] shows that our VG–based strategy gives similar results in terms of molecular vibrations coupled to the electronic excitation, and also in terms of relative intensities of the various regions. Results obtained from MD–based approaches describing the same system[4,12,30] show rather different profiles for $\omega > 1000$cm^{-1}, overestimating the effect of modes in the 1300–1600 cm^{-1} region

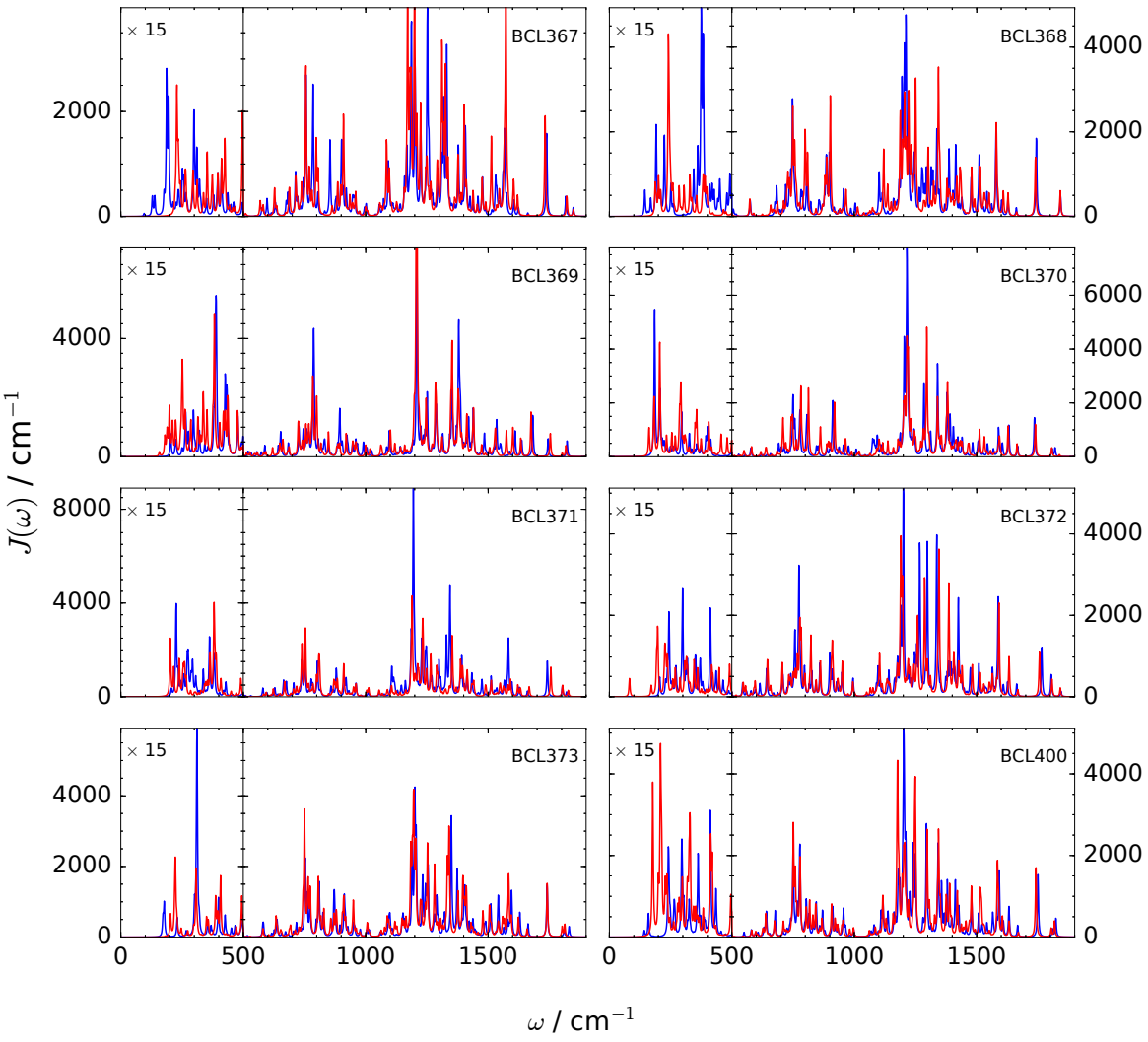

Figure 1: Comparison between calculated spectral densities at $t = 0$ ns (blue line) and $t = 8$ ns (red line), with broadening parameter $\gamma = 5$ cm^{-1}.

because of the problematic treatment of quantised vibrations in classical simulations,[11] as mentioned in the Introduction. A more sophisticated QM/MM MD approach describing structurally similar chromophores in a different protein environment,[14] is qualitatively in agreement with our calculations.

We highlight how this calculation strategy allows to study quickly the changes of the spectral density over large time scales, which cannot be easily done with MD–based approaches: averaging over different conformations explored on such time scales would not be correct, as the energy transfer process occurs in one of the possible conformations exclusively. Additionally, the computational cost of an MD–based approach applied to such time scales would make the calculations impossible. The equivalent alternative using an MD–based approach would consist of repeating a few thousands TDDFT calculations on portions of trajectory separated in time, which clearly makes the procedure extremely costly. In summary, we highlight a computational insight that cannot be achieved with other methods and, consequently, a mechanistic insight which is not present in literature. To support this perspective, in Fig. 2 we show the repeated calculation of the spectral density at various points along the trajectory for BCL367. We notice how the time evolution of the spectral density has a significant influence on the intramolecular modes at $\omega \leq 500$ cm^{-1}. We also observe minor redistributions of the coupling with modes at 1200–1400 cm^{-1}, and considerable changes at ≈ 1600 cm^{-1}, but, as commonly assumed and demonstrated in the second part of this paper, these modes have a low impact on the exciton dynamics.

The objective at this point is to build the best possible phenomenological model of the excitonic system retaining the most important information of the spectral density. We start by constructing a coarser representation of the spectral density based on a reduced number of modes but still able to capture the shape of the spectral density and differentiate between the spectral densities of the different chromophores. We fit the broadened spectral density with the sum of the spectral densities of 4 damped harmonic oscillators, each with a characteristic frequency ω_k, damping (broadening) γ_k and intensity A_k, as in

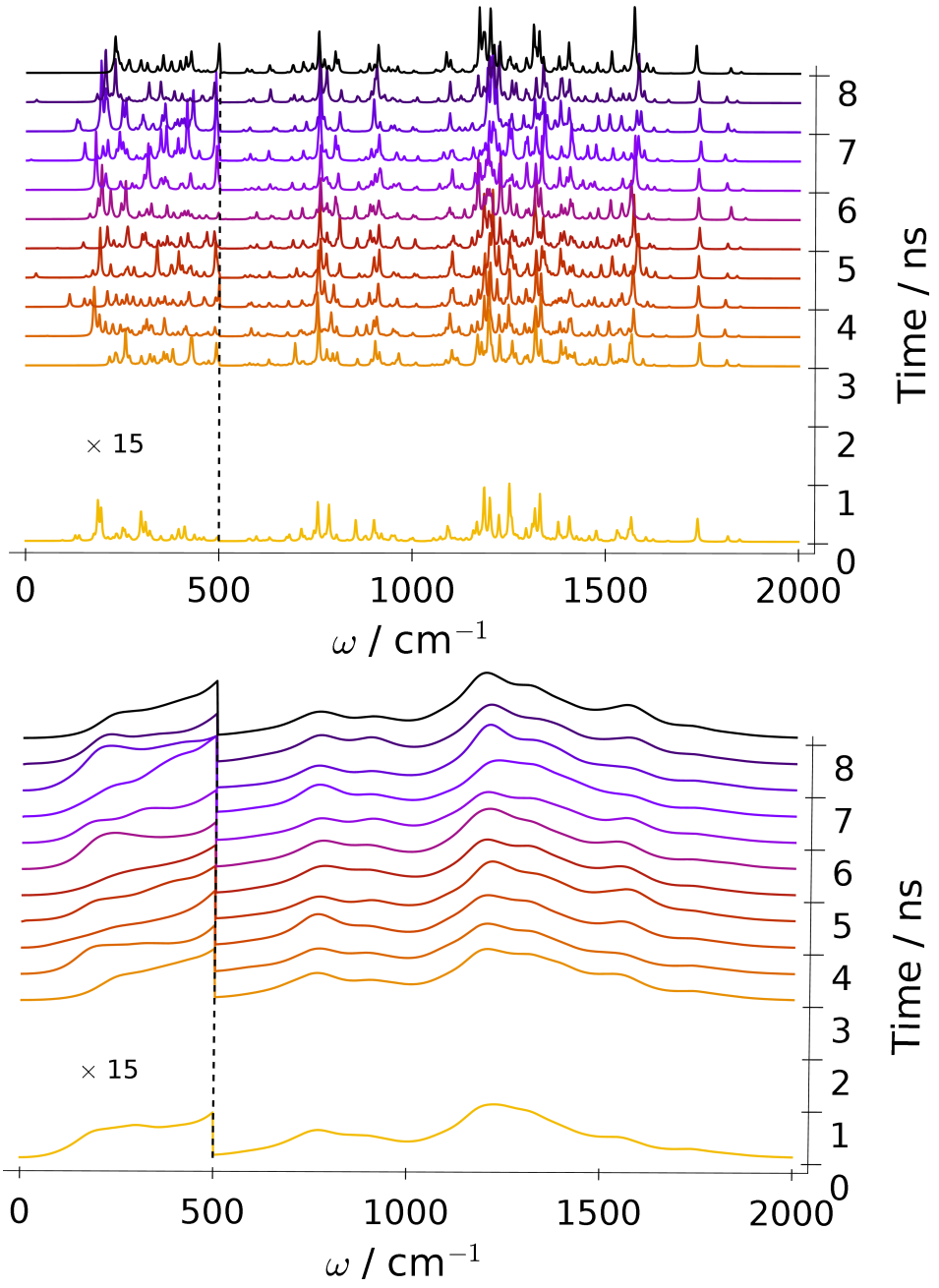

Figure 2: Comparison between calculated spectral densities at various times for BCL367, with broadening parameter $\gamma = 5$ cm^{-1} (top) and $\gamma = 125$ cm^{-1} (bottom).

$$J(\omega) = \sum_{k=1}^{4} A_k \frac{\gamma_k \omega^2}{(\gamma_k \omega)^2 + (\omega_k^2 - \omega^2)^2}, \tag{7}$$

where we fit the parameters A_k, γ_k, and ω_k. We imposed constraints in terms of allowed intervals for each ω_k, setting 0 cm^{-1} $< \omega_1 <$ 500 cm^{-1}, 500 cm^{-1} $< \omega_2 <$ 1000 cm^{-1}

and $\omega_3, \omega_4 > 1000$ cm^{-1}, which seemed reasonable intervals, considering the coarse spectral densities reported in Figs. 2–3. We introduced constraints because the high intensity region is not necessarily the most important one but, as we will see below, it also depends on the energy range of the excitonic system. It is important that the approximate spectral densities correctly sample all frequency ranges, while an unconstrained fit would describe better the regions at higher intensity. In Fig. 3 we report the broadened and fitted spectral densities, from which we obtained the Huang–Rhys factor of the k-th effective mode S_k.

$$\begin{aligned} \lambda_k &= \frac{1}{\pi} \int_0^\infty \frac{J_k(\omega)}{\omega} \, \mathrm{d}\omega \\ S_k &= \frac{\lambda_k}{\omega_k}. \end{aligned} \tag{8}$$

The total fitted reorganisation energies ($\lambda_{fit} = \sum_{k=1}^{4} \lambda_k$) are slightly lower ($\approx 10$cm^{-1}) with respect to the ones obtained from the previously discussed normal modes analysis, thus we rescaled them to match the values reported in Table 1 for the exciton dynamics calculations.

The coarse spectral densities reported in the bottom panel of Fig. 2 highlight more clearly how the time evolution has no significant impact on the $\omega > 500$ cm^{-1} region, while it is non negligible in the $\omega \leq 500$ cm^{-1} one, resulting in a shift of several wavenumbers of the effective frequency describing this region, and thus potentially impacting the exciton dynamics. In Table 2 we report a summary of the evolution of the effective modes along the MD trajectory for BCL367, based on the broad spectral densities reported in the bottom panel of Fig. 2. These data highlight that the time evolution has a high influence on the intramolecular modes in the ω_1 region, showing a huge change in the position of the effective mode over the 210–350 cm^{-1} range. Modes in the ω_2 region are affected to a much lesser extent, showing a homogeneous behaviour along the trajectory. Modes in the $\omega_{3,4}$ regions are somehow reciprocally influenced depending on the presence of an effective mode above 1500

cm^{-1}: when $\omega_4 > 1500$ cm^{-1}, $S_3 \gg S_4$. When $\omega_4 < 1500$ cm^{-1}, S_3 and S_4 are comparable. However, the effective frequencies in these regions behave homogeneously as well.

Table 2: Results from the fitting of broadened spectral densities ($\gamma = 125$ cm^{-1}) for BCL367 along the MD trajectory. Time in ns, ω_k and γ_k in cm^{-1}, S_k dimensionless.

Time	ω_1	γ_1	S_1	ω_2	γ_2	S_2	ω_3	γ_3	S_3	ω_4	γ_4	S_4
0.0	224.39	167.06	0.0306	787.79	258.80	0.0583	1210.59	172.63	0.0186	1320.01	391.87	0.0399
3.0	281.45	152.67	0.0137	776.19	263.79	0.0589	1200.34	173.91	0.0210	1360.12	400.79	0.0390
3.5	216.54	184.02	0.0344	789.27	276.01	0.0554	1195.53	180.10	0.0205	1335.33	402.34	0.0366
4.0	291.47	414.15	0.0232	773.11	198.21	0.0568	1248.29	328.72	0.0604	1557.52	150.78	0.0049
4.5	286.68	333.07	0.0276	783.26	249.19	0.0490	1252.42	302.99	0.0608	1561.23	185.24	0.0088
5.0	276.03	195.40	0.0152	796.72	248.41	0.0591	1253.85	325.10	0.0614	1551.68	152.35	0.0057
5.5	228.36	170.61	0.0367	794.84	254.01	0.0592	1224.45	240.97	0.0500	1481.72	349.49	0.0157
6.0	240.71	204.40	0.0253	811.05	315.02	0.0576	1195.55	148.48	0.0156	1343.30	419.76	0.0428
6.5	351.57	377.87	0.0342	781.22	245.27	0.0624	1213.04	159.65	0.0164	1334.34	370.48	0.0462
7.0	239.87	255.10	0.0576	781.82	239.63	0.0466	1200.92	110.06	0.0158	1322.74	398.94	0.0520
7.5	222.03	124.94	0.0232	800.86	295.12	0.0673	1207.50	156.07	0.0244	1375.79	429.56	0.0373
8.0	300.88	298.15	0.0209	770.88	229.88	0.0501	1234.96	309.28	0.0694	1562.64	174.78	0.0082

In Table 3 we report a summary of the effective modes we extracted with this fitting procedure. In the ω_1 region, we obtain effective frequencies in the 240–300 cm^{-1} range, with the exception of BCL369. BCL400 is the only one showing the largest Huang–Rhys factor in this region. In the ω_2–ω_4 regions, the behaviour of the various chromophores is pretty much similar. The only exception in this homogeneous behaviour is BCL367, which is the only chromophore showing a maximum above 1500 cm^{-1}. Overall, we observe a consistent picture arising from the coarse graining of the spectral densities, and we do not expect significant differences among chromophores at this point. To confirm this hypothesis, we studied the exciton dynamics of the system, and our results are discussed in the next sections.

2.2 Exciton dynamics

In this section we study the exciton dynamics using the effective modes extracted from the spectral densities in Sec. 2.1. We first establish whether the differences in the exciton-vibrational coupling for different chromophores are significant and what the most important component is for the construction of the model Hamiltonian. As we want to isolate the effect

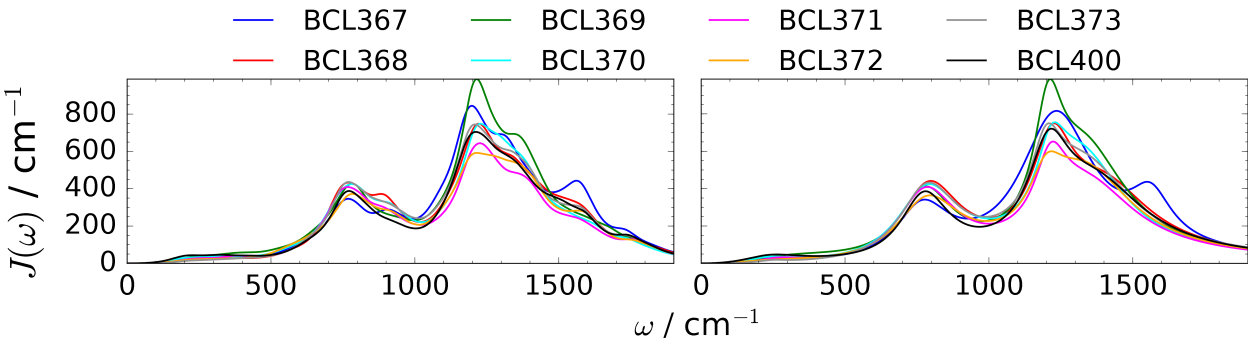

Figure 3: Left: calculated spectral densities ($t = 8$ ns) with broadening parameter $\gamma = 125$ cm^{-1}. Right: fitted spectral densities (see Eq. 7) used to extract effective modes, summarised in Table 3.

Table 3: Results from the fitting of broadened spectral densities ($\gamma = 125$ cm^{-1}). ω_k and γ_k in cm^{-1}, S_k dimensionless.

	ω_1	γ_1	S_1	ω_2	γ_2	S_2	ω_3	γ_3	S_3	ω_4	γ_4	S_4
BCL367	300.88	298.15	0.0209	770.88	229.88	0.0501	1234.96	309.28	0.0694	1562.64	174.78	0.0082
BCL368	242.41	108.44	0.0205	794.68	257.77	0.0744	1220.08	175.40	0.0290	1407.96	389.34	0.0290
BCL369	352.68	505.15	0.0555	780.76	228.73	0.0611	1207.15	117.51	0.0229	1336.75	347.33	0.0466
BCL370	243.05	205.42	0.0415	790.14	264.03	0.0728	1216.89	123.46	0.0133	1327.38	348.18	0.0440
BCL371	271.50	180.39	0.0252	783.19	250.54	0.0689	1214.97	135.86	0.0154	1349.34	403.36	0.0351
BCL372	277.42	429.20	0.0278	790.26	273.38	0.0630	1200.20	141.26	0.0117	1340.24	389.80	0.0418
BCL373	249.19	124.50	0.0106	788.84	248.38	0.0698	1199.56	131.05	0.0162	1335.10	401.22	0.0460
BCL400	253.10	259.79	0.0653	777.33	206.68	0.0541	1208.25	173.99	0.0264	1378.26	416.03	0.0340
Exp.[48]	306.50	417.21	0.0737	759.49	235.32	0.0978	1218.09	362.51	0.0815			

of intramolecular (high frequency) modes, we include them in the system and we ignore the effect of the bath (which may mask some of the effect and would require additional parameters).

2.2.1 Hamiltonian of the vibronically coupled system

To describe the exciton dynamics of the FMO complex, where effective intramolecular vibrational modes are explicitly included in the system Hamiltonian, we consider one electronic state per monomer. Here each electronic state can be in principle coupled to any arbitrary number of intramolecular vibrational modes, which are assumed to be localized on a monomer. The Hamiltonian of the vibronically coupled system can then be written in a site basis as follows:[51]

$$\hat{H} = \sum_{i,\boldsymbol{v}} \big(E_i + \hbar\boldsymbol{\omega}\cdot\boldsymbol{v}\big)|i,\boldsymbol{v}\rangle\langle i,\boldsymbol{v}| + \sum_{i,j\neq i}\sum_{\boldsymbol{v},\boldsymbol{w}} \tau_{ij} V^{i,j}_{\boldsymbol{v},\boldsymbol{w}} |i,\boldsymbol{v}\rangle\langle j,\boldsymbol{w}|, \tag{9}$$

where E_i is the excitation energy localized on molecule i with zero-point energy included; $\boldsymbol{\omega}$ and $\boldsymbol{v}$ are the vectors of vibrational frequency and vibrational quantum number, respectively, of vibronic state $|i,\boldsymbol{v}\rangle$, where a monomer i is in its electronic excited state and the other monomers are in their electronic ground state; τ_{ij} is the excitonic coupling between states i and j; and $V^{i,j}_{\boldsymbol{v},\boldsymbol{w}} = \prod_m \mathcal{S}^{i,j}_{v_m,w_m}$ is the Franck-Condon factor, where $\mathcal{S}^{i,j}_{v_m,w_m}$ is the vibrational overlap integral for the vibrational mode m associated with molecule i or j and determined by the Huang-Rhys factor $S^{i,j}_m$ and the vibrational quantum numbers v_m and w_m.[52] (Note that the $\mathcal{S}^{i,j}_{v_m,w_m}$ is zero if m is not localized on i or j.)

We employ an eight-site model of the FMO complex and use the matrix elements in refs.[53,54] for the excitation energies E_i and the excitonic coupling τ_{ij} given by in cm^{-1}

$$\hat{H}_{\mathrm{Exciton}} = \begin{pmatrix} 310 & -98 & 6 & -6 & 7 & -12 & -10 & 38 \\ -98 & 230 & 30 & 7 & 2 & 12 & 5 & 8 \\ 6 & 30 & 0 & -59 & -2 & -10 & 5 & 2 \\ -6 & 7 & -59 & 180 & -65 & -17 & -65 & -2 \\ 7 & 2 & -2 & -65 & 405 & 89 & -6 & 5 \\ -12 & 11 & -10 & -17 & 89 & 320 & 32 & -10 \\ -10 & 5 & 5 & -64 & -6 & 32 & 270 & -11 \\ 38 & 8 & 2 & -2 & 5 & -10 & -11 & 505 \end{pmatrix} \tag{10}$$

Each site is coupled to four effective vibrational modes extracted from the spectral density of each chromophore (see Table 3) unless noted otherwise. The dimension of the Hilbert space increases rapidly with the increase of the vibrational quantum number. Since it is not likely that vibronic states with a large quantum number are populated by a substantial amount, we impose a cut-off for the vibrational quantum number as discussed in detail in the next

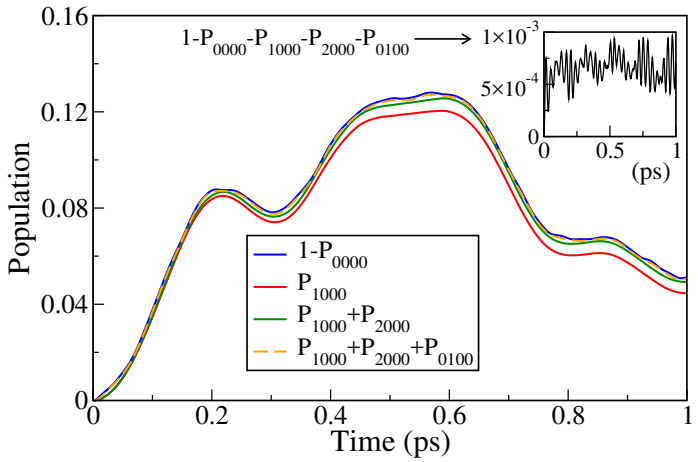

Figure 4: Population of the vibrational excited states with a maximum total quantum number of 2. Total population of the low-lying vibrational excited states almost amounts to the total population of the vibrational excited states, i.e., $P_{1000} + P_{2000} + P_{0100} \approx 1 - P_{0000}$. The inset shows that higher excited states have negligible population ($1 - P_{0000} - P_{1000} - P_{2000} - P_{0100} < 1{\times}10^{-3}$) and therefore can be truncated.

section. We assume an instantaneous excitation of site i=8 (BCL400), which has the largest excitation energy, in its vibrational ground state at t=0. The time evolution of the initial state is obtained by $|\psi(t)\rangle = e^{-i\hat{H}t/\hbar}|\psi(0)\rangle$, where the time evolution operator is expanded using Chebychev polynomials.[55–57]

2.2.2 Impact of site-dependent spectral densities on exciton dynamics

Table 3 shows that the strongest exciton-vibrational coupling appears at high frequency modes ($\omega > 770$ cm^{-1}) except for BCL400, where the lowest frequency mode exhibits the strongest coupling. However, the vibrational energy of high frequency modes is much larger than the excitonic transition energy and therefore the amount of population transferred to these states may still be insignificant. To find which effective modes contribute most to the exciton dynamics, we analyze how the population is distributed among different vibronic states for 1 ps with a maximum total vibrational quantum number of 2 (note that 1 ps is the relevant time window in the LHC exciton dynamics,[58,59] and our result, as described below, suggests that a cut-off of total vibrational quanta to 2 is good enough to this end). Fig. 4 illustrates that most of the population of the vibrational excited states is distributed among

the low-lying vibrational excited states. (In the figure, P_{n000} / P_{0100} denotes the total population of the vibrational excited states with the lowest / 2^{nd} lowest frequency mode excited by n quanta / one quantum while all other modes kept in the ground state, and P_{0000} is the total population of the vibrational ground states.) We find that the excitation of the lowest frequency mode by up to two quanta (with all other modes in the ground state) and excitation of the 2^{nd} lowest frequency mode by one quantum can account for the total population of the vibrational excited states, i.e., $P_{1000} + P_{2000} + P_{0100} \approx 1 - P_{0000}$. This indicates that the population of the vibrational excited states of high frequency modes is negligible despite the large Huang-Rhys factor. In fact, the maximum value of $P_{1000}, P_{0100}, P_{0010}$, and P_{0001} over 1 ps time window is 1.2×10^{-1}, 2.3×10^{-3}, 5.8×10^{-4}, and 1.9×10^{-4}, respectively. As well, the population of the excited states decreases rapidly increasing of the quantum number, *e.g.* P_{1000}=0.95, P_{2000}=0.04, and P_{3000}=0.005 at t=1 ps. Our result suggests that the exciton dynamics can be studied with high frequency modes (those with frequencies ω_3 and ω_4) kept in the ground state and the vibrational quantum number of the low frequency mode restricted to small number. (Note that keeping high frequency modes in the ground state is not the same as neglecting exciton-vibrational coupling with high frequency modes because the effective excitonic coupling is still modulated by the Franck-Condon factor.) Therefore, we set the maximum vibrational quantum number of the modes ($\omega_1, \omega_2, \omega_3, \omega_4$) in Table 3 to (2, 1, 0, 0) and restrict the maximum total vibrational quantum number to 2 to study the impact of site–dependent spectral densities on exciton dynamics.

To determine whether the differences in the exciton-vibrational coupling for different chromophore are significant, we obtain the population dynamics using a model Hamiltonian, where each site is coupled to four vibrational modes with the same frequency and Huang-Rhys factor for each chromophore. We use 8 possible values for the exciton-vibrational coupling corresponding to each of the 8 spectral densities given in Table 3. In Fig. 5 we compare the population evolution with uniform spectral density with the population evolution where each chromophore has a different coupling with the vibrations. Broadly speaking, our results

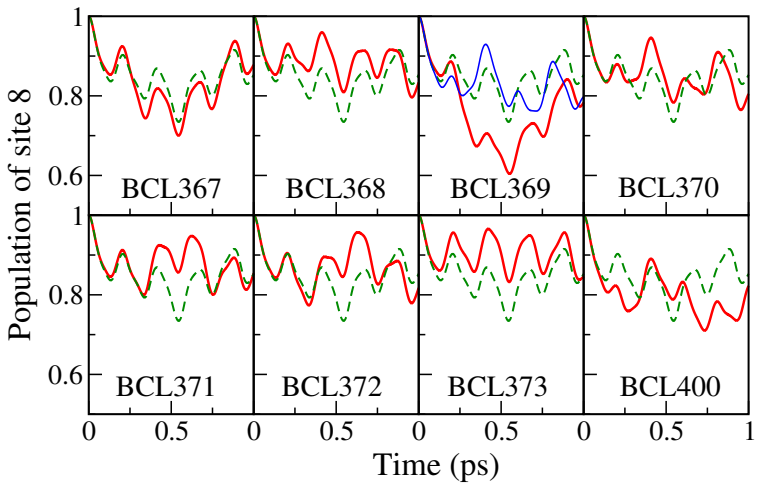

Figure 5: Time evolution of the population of site 8 (BCL400). Each panel corresponds to employing the spectral density of different chromophores with all sites coupled to the same effective modes. Results using different spectral densities on each site are plotted as dashed lines.

suggest that the differences in the exciton-vibrational coupling for different chromophores are not too significant in terms of exciton dynamics when a reduced model of the spectral density is employed and that in most cases one can assume the same exciton-vibrational coupling on all sites to study the quantum dynamics of the FMO complex.

It should be noted, however, that although the details of the spectral density seem unimportant in the exciton dynamics, some differences in exciton-vibrational coupling are more influential than others. The differences in the low frequency modes, of which vibrational energy is closer to the excitonic transition energy, have more impact on the exciton dynamics, which explains why the population dynamics using the spectral density of chromophore BCL369 is somewhat different from the rest (note that ω_1 is much higher for BCL369 (353 cm^{-1}) as compared to other chromophores). Replacing the ω_1 of the spectral density of BCL369 with that of BCL370 (243 cm^{-1}) leads to a population dynamics very similar to the rest (see thin blue line in Fig. 5). On the other hand, the differences in exciton-vibrational coupling for high frequency modes are not very important. For example, BCL367 has the largest Huang-Rhys factor S for ω_3, whereas BCL372 has the smallest S for ω_3, but their population dynamics is not significantly different from each other. Our result confirms that the

difference in the spectral density for the low frequency part has more impact on the dynamics even if the exciton-vibrational coupling is much smaller than that of high frequency modes and therefore care needs to be taken for the description of the exciton-vibrational coupling in the low frequency region.

3 Conclusions

We adopted a fast and accurate method to calculate the intramolecular part of the spectral density of a chromophore embedded in its environment, based on the normal modes analysis proposed recently by Lee and Coker[28,29] and combining it with the Vertical Gradient approximation.[35–38] This allows a significant reduction in the computational effort with respect to the methods proposed previously, retaining the accuracy guaranteed by QM–based approaches. Additionally, we highlighted in the discussion a new aspect in terms of access to computational insight regarding conformational changes that occur over large time scales, which showed a significant influence on the intramolecular modes that have large effects on the exciton dynamics. We extracted effective frequencies from our spectral densities to check the impact of the coupling of the electronic excitation with intramolecular modes on the exciton dynamics of the system. The dynamics obtained using an eight-site model suggests that the differences in exciton-vibrational coupling for different chromophores are not significant in terms of exciton dynamics and high frequency modes with much larger vibrational energy than the excitonic transition energy have negligible influence on exciton dynamics despite the large Huang-Rhys factor. While this was commonly assumed throughout the literature, our calculations confirm it without any prior assumption. The oscillatory behaviour is excitonic rather than vibronic, and the small changes can be ascribed to the small importance of the vibronic part rather than the details of the spectral density. As a side note, the method adopted is of general interest for the description of excitation dynamics, as other proteins[60,61] and phenomena[62,63] exist in which high frequency intramolecular vibrations play a central

role.

Furthermore, our results provide useful information concerning the sampling needed for MD–based approaches to obtain the spectral density (in particular regarding the time separation between snapshots, which determines the highest sampled frequency). In fact, we do not expect the intermolecular modes to influence the spectral density above 500 cm^{-1}, and we showed that this region is virtually identical for identical chromophores. The main findings of this work will be useful to guide the development of model Hamiltonians for light harvesting complexes that retain only information on the system that is essential to describe the exciton physics.

4 Computational Details

Starting structure. We obtained the crystal structure of FMO from the Protein Data Bank (PDB: 3BSD). We prepared the system for the QM simulations with the GROMACS 5.0.5 software.[64] The protein was embedded in a cubic box of suitable dimensions. Histidine residues have been assigned the appropriate protonation state to allow coordinating Mg atoms of BCLs, otherwise they have been assigned the proton in position ε. We added water molecules and we set the ionic strength of the starting box to 150 mM by adding the appropriate number of potassium and chloride ions. The system has been described using the TIP3P model for water molecules, the CHARMM36 force field for the protein,[65] and literature parameters for the BCLs.[66] We initially minimised the system keeping all BCLs frozen, with 2000 steps of Steepest Descent. For all the following steps, we used an integration step of 2 fs and constrained all the bonds with the LINCS algorithm implemented in GROMACS.[67] We then equilibrated the system in two steps of 500 ps each, run in NVT (heating up to 300K) and NPT conditions (Berendsen barostat) respectively. Finally, we ran 8 separate equilibrations of several nanoseconds, in which each one of the 8 chromophores in one of the 3 monomeric units of FMO was kept frozen. For the following QM analysis, a

series of snapshots from the last portion of the trajectory were picked for each chromophore.

QM calculations. Starting from the snapshots extracted, we reduced the number of atoms for our following calculations by keeping only the residues within 8 Å of the frozen chromophore. For all the following calculations we used a two-layer ONIOM scheme, using (TD)DFT/B3LYP/6-31G* for the QM region and UFF parameters for the MM region. The number of atoms of BCLs chromophores in the QM region has been reduced from 140 to 85 by inserting a link atom between the first and second Carbon atoms of the Phythyl chain. Geometry optimisations were run keeping the atoms belonging to the protein backbone fixed, to preserve a configuration as close as possible to the one in the protein. On the optimised systems, we computed vibrational frequencies (only for the QM region) and excited state gradients. All calculations were run using the Gaussian09 package.[68]

Acknowledgement

This work was supported by ERC through Grant No. 615834. We are grateful to Dr. Fabrizio Santoro (ICCOM–CNR Pisa, Italy) and Dr. Yun Geng (Northeast Normal University, China) for access to computational resources, and to Dr. Ana Damjanović (Johns Hopkins, USA) for the CHARMM parameters of BCL chromophores.

References

(1) Curutchet, C.; Mennucci, B. Quantum Chemical Studies of Light Harvesting. *Chem. Rev.* **2017**, *117*, 294–343.

(2) Mirkovic, T.; Ostroumov, E. E.; Anna, J. M.; van Grondelle, R.; Govindjee,; Scholes, G. D. Light Absorption and Energy Transfer in the Antenna Complexes of Photosynthetic Organisms. *Chem. Rev.* **2017**, *117*, 249–293.

(3) Scholes, G. D.; Fleming, G. R.; Olaya-Castro, A.; van Grondelle, R. Lessons from nature about solar light harvesting. *Nat. Chem.* **2011**, *3*, 763–774.

(4) Wang, X.; Ritschel, G.; Wuster, S.; Eisfeld, A. Open quantum system parameters for light harvesting complexes from molecular dynamics. *Phys. Chem. Chem. Phys.* **2015**, *17*, 25629–25641.

(5) Olbrich, C.; Jansen, T. L. C.; Liebers, J.; Aghtar, M.; Strümpfer, J.; Schulten, K.; Knoester, J.; Kleinekathöfer, U. From Atomistic Modeling to Excitation Transfer and Two-Dimensional Spectra of the FMO Light-Harvesting Complex. *J. Phys. Chem. B* **2011**, *115*, 8609–8621.

(6) Schmidt am Busch, M.; Müh, F.; El-Amine Madjet, M.; Renger, T. The Eighth Bacteriochlorophyll Completes the Excitation Energy Funnel in the FMO Protein. *J. Phys. Chem. Lett.* **2011**, *2*, 93–98.

(7) Higashi, M.; Saito, S. Quantitative Evaluation of Site Energies and Their Fluctuations of Pigments in the Fenna–Matthews–Olson Complex with an Efficient Method for Generating a Potential Energy Surface. *J. Chem. Theory Comput.* **2016**, *12*, 4128–4137.

(8) Jia, X.; Mei, Y.; Zhang, J. Z.; Mo, Y. Hybrid QM/MM study of FMO complex with polarized protein-specific charge. *Sci. Rep.* **2015**, *5*, 17096.

(9) Gao, J.; Shi, W.-J.; Ye, J.; Wang, X.; Hirao, H.; Zhao, Y. QM/MM Modeling of Environmental Effects on Electronic Transitions of the FMO Complex. *J. Phys. Chem. B* **2013**, *117*, 3488–3495.

(10) Shim, S.; Rebentrost, P.; Valleau, S.; Aspuru-Guzik, A. Atomistic Study of the Long-Lived Quantum Coherences in the Fenna-Matthews-Olson Complex. *Biophys. J.* **2012**, *102*, 649–660.

(11) Renger, T.; Klinger, A.; Steinecker, F.; Schmidt am Busch, M.; Numata, J.; Müh, F. Normal Mode Analysis of the Spectral Density of the Fenna–Matthews–Olson Light-Harvesting Protein: How the Protein Dissipates the Excess Energy of Excitons. *J. Phys. Chem. B* **2012**, *116*, 14565–14580.

(12) Aghtar, M.; Strümpfer, J.; Olbrich, C.; Schulten, K.; Kleinekathöfer, U. The FMO Complex in a Glycerol–Water Mixture. *J. Phys. Chem. B* **2013**, *117*, 7157–7163.

(13) Jurinovich, S.; Curutchet, C.; Mennucci, B. The Fenna–Matthews–Olson Protein Revisited: A Fully Polarizable (TD)DFT/MM Description. *ChemPhysChem* **2014**, *15*, 3194–3204.

(14) Rosnik, A. M.; Curutchet, C. Theoretical Characterization of the Spectral Density of the Water-Soluble Chlorophyll-Binding Protein from Combined Quantum Mechanics/Molecular Mechanics Molecular Dynamics Simulations. *J. Chem. Theory Comput.* **2015**, *11*, 5826–5837.

(15) Ishizaki, A.; Fleming, G. R. Theoretical Examination of Quantum Coherence in a Photosynthetic System at Physiological Temperature. *Proc. Natl. Acad. Sci. USA* **2009**, *106*, 17255–17260.

(16) Mohseni, M.; Rebentrost, P.; Lloyd, S.; Aspuru-Guzik, A. Environment-Assisted Quantum Walks in Photosynthetic Energy Transfer. *J. Chem. Phys.* **2008**, *129*, 174106.

(17) Rebentrost, P.; Mohseni, M.; Kassal, I.; Lloyd, S.; Aspuru-Guzik, A. Environment-Assisted Quantum Transport. *New J. Phys.* **2009**, *11*, 033003.

(18) Plenio, M. B.; Huelga, S. F. Dephasing-Assisted Transport: Quantum Networks and Biomolecules. *New J. Phys.* **2008**, *10*, 113019.

(19) Caruso, F.; Chin, A. W.; Datta, A.; Huelga, S. F.; Plenio, M. B. Highly Efficient Energy Excitation Transfer in Light-Harvesting Complexes: The Fundamental Role of Noise-Assisted Transport. *J. Chem. Phys.* **2009**, *131*, 105106.

(20) Chin, A. W.; Datta, A.; Caruso, F.; Huelga, S. F.; Plenio, M. B. Noise-Assisted Energy Transfer in Quantum Networks and Light-Harvesting Complexes. *New J. Phys.* **2010**, *12*, 065002.

(21) Kolli, A.; O'Reilly, E. J.; Scholes, G. D.; Olaya-Castro, A. The Fundamental Role of Quantized Vibrations in Coherent Light Harvesting by Cryptophyte Algae. *J. Chem. Phys.* **2012**, *137*, 174109.

(22) Novelli, F.; Nazir, A.; Richards, G. H.; Roozbeh, A.; Wilk, K. E.; Curmi, P. M. G.; Davis, J. A. Vibronic Resonances Facilitate Excited-State Coherence in Light-Harvesting Proteins at Room Temperature. *J. Phys. Chem. Lett.* **2015**, *6*, 4573–4580.

(23) Chenu, A.; Christensson, N.; Kauffmann, H. F.; Mančal, T. Ground-State Vibrational Coherences in 2D Spectra of Photosynthetic Complexes. *Sci. Rep.* **2013**, *3*, 02029.

(24) Chin, A. W.; Prior, J.; Rosenbach, R.; Caycedo-Soler, F.; Huelga, S. F.; Plenio, M. B. The Role of Non-Equilibrium Vibrational Structures in Electronic Coherence and Recoherence in Pigment-Protein Complexes. *Nature Phys.* **2013**, *9*, 113–118.

(25) Lim, J.; Paleček, D.; Caycedo-Soler, F.; Lincoln, C. N.; Prior, J.; von Berlepsch, H.; Huelga, S. F.; Plenio, M. B.; Zigmantas, D.; Hauer, J. Vibronic Origin of Long-lived Coherence in an Artificial Molecular Light Harvester. *Nature Commun.* **2015**, *6*, 7755.

(26) Tiwari, V.; Peters, W. K.; Jonas, D. M. Electronic Resonance with Anticorrelated Pigment Vibrations Drives Photosynthetic Energy Transfer outside the Adiabatic Framework. *Proc. Natl. Acad. Sci. USA* **2013**, *110*, 1203–1208.

(27) Plenio, M. B.; Almeida, J.; Huelga, S. F. Origin of Long-Lived Oscillations in 2D-Spectra of a Quantum Vibronic Model: Electronic versus Vibrational Coherence. *J. Chem. Phys.* **2013**, *139*, 235102.

(28) Lee, M. K.; Coker, D. F. Modeling Electronic-Nuclear Interactions for Excitation Energy Transfer Processes in Light-Harvesting Complexes. *J. Phys. Chem. Lett.* **2016**, *7*, 3171–3178.

(29) Lee, M. K.; Huo, P.; Coker, D. F. Semiclassical Path Integral Dynamics: Photosynthetic Energy Transfer with Realistic Environment Interactions. *Ann. Rev. Phys. Chem.* **2016**, *67*, 639–668.

(30) Chandrasekaran, S.; Aghtar, M.; Valleau, S.; Aspuru-Guzik, A.; Kleinekathöfer, U. Influence of Force Fields and Quantum Chemistry Approach on Spectral Densities of BChl a in Solution and in FMO Proteins. *J. Phys. Chem. B* **2015**, *119*, 9995–10004.

(31) Jing, Y.; Zheng, R.; Li, H.-X.; Shi, Q. Theoretical Study of the Electronic–Vibrational Coupling in the Qy States of the Photosynthetic Reaction Center in Purple Bacteria. *J. Phys. Chem. B* **2012**, *116*, 1164–1171.

(32) Padula, D.; Jurinovich, S.; Di Bari, L.; Mennucci, B. Simulation of Electronic Circular Dichroism of Nucleic Acids: From the Structure to the Spectrum. *Chem. Eur. J.* **2016**, *22*, 17011–17019.

(33) Prandi, I. G.; Viani, L.; Andreussi, O.; Mennucci, B. Combining classical molecular dynamics and quantum mechanical methods for the description of electronic excitations: The case of carotenoids. *J. Comput. Chem.* **2016**, *37*, 981–991.

(34) Do, H.; Troisi, A. Developing accurate molecular mechanics force fields for conjugated molecular systems. *Phys. Chem. Chem. Phys.* **2015**, *17*, 25123–25132.

(35) Avila Ferrer, F. J.; Santoro, F. Comparison of vertical and adiabatic harmonic approaches for the calculation of the vibrational structure of electronic spectra. *Phys. Chem. Chem. Phys.* **2012**, *14*, 13549–13563.

(36) Santoro, F.; Jacquemin, D. Going beyond the vertical approximation with time-dependent density functional theory. *Wiley Interdisciplinary Reviews: Computational Molecular Science* **2016**, *6*, 460–486.

(37) Macak, P.; Luo, Y.; Ågren, H. Simulations of vibronic profiles in two-photon absorption. *Chem. Phys. Lett.* **2000**, *330*, 447 – 456.

(38) Hazra, A.; Chang, H. H.; Nooijen, M. First principles simulation of the UV absorption spectrum of ethylene using the vertical Franck-Condon approach. *J. Chem. Phys.* **2004**, *121*, 2125–2136.

(39) Padula, D.; Lahoz, I. R.; Díaz, C.; Hernández, F. E.; Di Bari, L.; Rizzo, A.; Santoro, F.; Cid, M. M. A Combined Experimental–Computational Investigation to Uncover the Puzzling (Chiro-)optical Response of Pyridocyclophanes: One- and Two-Photon Spectra. *Chem. Eur. J.* **2015**, *21*, 12136–12147.

(40) Liu, Y.; Cerezo, J.; Santoro, F.; Rizzo, A.; Lin, N.; Zhao, X. Theoretical investigation of the broad one-photon absorption line-shape of a flexible symmetric carbazole derivative. *Phys. Chem. Chem. Phys.* **2016**, *18*, 22889–22905.

(41) Padula, D.; Di Bari, L.; Santoro, F.; Gerlach, H.; Rizzo, A. Analysis of the Electronic Circular Dichroism Spectrum of (–)[9](2, 5) Pyridinophane. *Chirality* **2012**, *24*, 994–1004.

(42) Andrushchenko, V.; Padula, D.; Zhivotova, E.; Yamamoto, S.; Bouř, P. Magnetic Circular Dichroism of Porphyrin Lanthanide M3+ Complexes. *Chirality* **2014**, *26*, 655–662.

(43) Duschinsky, F. On the interpretation of electronic spectra of polyatomic molecules. I: the Franck-Condon principle. *Acta Physicochim. URSS* **1937**, *7*, 551–566.

(44) Neese, F.; Petrenko, T.; Ganyushin, D.; Olbrich, G. Advanced aspects of ab initio theoretical optical spectroscopy of transition metal complexes: Multiplets, spin-orbit coupling and resonance Raman intensities. *Coor. Chem. Rev.* **2007**, *251*, 288 – 327.

(45) Tomasi, J.; Mennucci, B.; Cammi, R. Quantum Mechanical Continuum Solvation Models. *Chem. Rev.* **2005**, *105*, 2999–3094.

(46) Klamt, A. The COSMO and COSMO-RS solvation models. *Wiley Interdisciplinary Reviews: Computational Molecular Science* **2011**, *1*, 699–709.

(47) Chung, L. W.; Sameera, W. M. C.; Ramozzi, R.; Page, A. J.; Hatanaka, M.; Petrova, G. P.; Harris, T. V.; Li, X.; Ke, Z.; Liu, F. et al. The ONIOM Method and Its Applications. *Chem. Rev.* **2015**, *115*, 5678–5796.

(48) Rätsep, M.; Freiberg, A. Electron–phonon and vibronic couplings in the {FMO} bacteriochlorophyll a antenna complex studied by difference fluorescence line narrowing. *J. Lumin.* **2007**, *127*, 251–259.

(49) Rätsep, M.; Cai, Z.-L.; Reimers, J. R.; Freiberg, A. Demonstration and interpretation of significant asymmetry in the low-resolution and high-resolution Qy fluorescence and absorption spectra of bacteriochlorophyll a. *J. Chem. Phys.* **2011**, *134*, 024506.

(50) Nitzan, A. *Chemical Dynamics in Condensed Phases*; Oxford University Press: New York, 2006.

(51) Lee, M. H.; Troisi, A. Vibronic Enhancement of Excitation Energy transport: Interplay

between Local and Non-Local Exciton-Phonon Interactions. *J. Phys. Chem.* **2017**, *146*, 075101.

(52) May, V.; Kühn, O. *Charge and Energy Transfer Dynamics in Molecular Systems*, 3rd ed.; Willey-VCH: Berlin, 2011.

(53) Schulze, J.; Shibl, M. F.; Al-Marri, M. J.; Kühn, O. Multi-Layer Multi-Configuration Time-Dependent Hartree Approach to the Correlated Exciton-Vibrational Dynamics in the FMO Complex. *J. Chem. Phys.* **2016**, *144*, 185101.

(54) Moix, J.; Wu, J.; Huo, P.; Coker, D.; Cao, J. Efficient Energy Transfer in Light-Harvesting Systems, III: The Influence of the Eighth Bacteriochlorophyll on the Dynamics and Efficiency in FMO. *J. Phys. Chem. Lett.* **2011**, *2*, 3045–3052.

(55) Tal-Ezer, H.; Kosloff, R. An Accurate and Efficient Scheme for Propagating the Time Dependent Schrödinger Equation. *J. Chem. Phys.* **1984**, *81*, 3967.

(56) Kosloff, R. Propagation Methods for Quantum Molecular Dynamics. *Annu. Rev. Phys. Chem.* **1994**, *45*, 145–178.

(57) Leforestier, C.; Bisseling, R. H.; Cerjan, C.; Feit, M. D.; Friesner, R.; Guldberg, A.; Hammerich, A.; Jolicard, G.; Karrlein, W.; Meyer, H.-D. et al. A Comparison of Different Propagation Schemes for the Time Dependent Schrödinger Equation. *J. Comput. Phys.* **1991**, *94*, 59–80.

(58) Christensson, N.; Kauffmann, H. F.; Pullerits, T.; Mančal, T. Origin of Long-Lived Coherences in Light-Harvesting Complexes. *J. Phys. Chem. B* **2012**, *116*, 7449–7454.

(59) Kreisbeck, C.; Kramer, T. Long-Lived Electronic Coherence in Dissipative Exciton Dynamics of Light-Harvesting Complexes. *J. Phys. Chem. Lett.* **2012**, *3*, 2828–2833.

(60) Kolli, A.; O'Reilly, E. J.; Scholes, G. D.; Olaya-Castro, A. The fundamental role of

quantized vibrations in coherent light harvesting by cryptophyte algae. *J. Chem. Phys.* **2012**, *137*, 174109.

(61) O'Reilly, E. J.; Olaya-Castro, A. Non-classicality of the molecular vibrations assisting exciton energy transfer at room temperature. *Nat. Comm.* **2014**, *5*, 3012.

(62) Christensson, N.; Milota, F.; Hauer, J.; Sperling, J.; Bixner, O.; Nemeth, A.; Kauffmann, H. F. High Frequency Vibrational Modulations in Two-Dimensional Electronic Spectra and Their Resemblance to Electronic Coherence Signatures. *J. Phys. Chem. B* **2011**, *115*, 5383–5391.

(63) Fujihashi, Y.; Chen, L.; Ishizaki, A.; Wang, J.; Zhao, Y. Effect of high-frequency modes on singlet fission dynamics. *J. Chem. Phys.* **2017**, *146*, 044101.

(64) Abraham, M. J.; Murtola, T.; Schulz, R.; Páll, S.; Smith, J. C.; Hess, B.; Lindahl, E. GROMACS: High performance molecular simulations through multi-level parallelism from laptops to supercomputers. *SoftwareX* **2015**, *1-2*, 19 – 25.

(65) Huang, J.; MacKerell, A. D. CHARMM36 all-atom additive protein force field: Validation based on comparison to NMR data. *J. Comput. Chem.* **2013**, *34*, 2135–2145.

(66) Damjanović, A.; Kosztin, I.; Kleinekathöfer, U.; Schulten, K. Excitons in a photosynthetic light-harvesting system: A combined molecular dynamics, quantum chemistry, and polaron model study. *Phys. Rev. E* **2002**, *65*, 031919.

(67) Hess, B. P-LINCS: A Parallel Linear Constraint Solver for Molecular Simulation. *J. Chem.Theory Comput.* **2008**, *4*, 116–122.

(68) Frisch, M. J.; Trucks, G. W.; Schlegel, H. B.; Scuseria, G. E.; Robb, M. A.; Cheeseman, J. R.; Scalmani, G.; Barone, V.; Mennucci, B.; Petersson, G. A. et al. Gaussian 09 Revision D.01. Gaussian Inc. Wallingford CT 2009.